

Whole-body Motion Planning and Safety-Critical Control for Aerial Manipulation

Lin Yang* Jinwoo Lee** Domenico Campolo* H. Jin Kim***
Jeonghyun Byun†***

* School of Mechanical and Aerospace Engineering, Nanyang Technological University, Singapore. (e-mail: yang0752@e.ntu.edu.sg, d.campolo@ntu.edu.sg)

** Department of Aerospace Engineering, Seoul National University, South Korea. (e-mail: jinwoolee0728@snu.ac.kr)

*** Automation and Systems Research Institute, Seoul National University, South Korea. (e-mail: {hjinkim, quswjdgs97}@snu.ac.kr)

Abstract: Aerial manipulation combines the maneuverability of multirotors with the dexterity of robotic arms to perform complex tasks in cluttered spaces. Yet planning safe, dynamically feasible trajectories remains difficult due to whole-body collision avoidance and the conservativeness of common geometric abstractions such as bounding boxes or ellipsoids. We present a whole-body motion planning and safety-critical control framework for aerial manipulators built on superquadrics (SQs). Using an SQ-plus-proxy representation, we model both the vehicle and obstacles with differentiable, geometry-accurate surfaces. Leveraging this representation, we introduce a maximum-clearance planner that fuses Voronoi diagrams with an equilibrium-manifold formulation to generate smooth, collision-aware trajectories. We further design a safety-critical controller that jointly enforces thrust limits and collision avoidance via high-order control barrier functions. In simulation, our approach outperforms sampling-based planners in cluttered environments, producing faster, safer, and smoother trajectories and exceeding ellipsoid-based baselines in geometric fidelity. Actual experiments on a physical aerial-manipulation platform confirm feasibility and robustness, demonstrating consistent performance across simulation and hardware settings. The video can be found at <https://youtu.be/hQYKwrWf1Ak>.

Keywords: Aerial manipulators, whole-body motion planning, collision avoidance, cluttered environments, Voronoi diagrams, safety-critical control.

1. INTRODUCTION

Aerial manipulation combines the maneuverability of unmanned aerial vehicles with the dexterity of robot arms. Leveraging this synergy, numerous studies have been conducted on diverse applications, including door opening (Lee et al. (2020)), plug-pulling (Byun et al. (2021)), non-destructive testing (NDT) (D’Angelo et al. (2025)), painting (Susbielle et al. (2025)), and pick-and-place (Blöchlinger et al. (2025)).

Bringing such applications into real-world operation requires prioritizing safety –most notably, preventing unintended collisions. This is especially important for aerial manipulators, whose end effectors can reach targets in tight or occluded spaces that would be inaccessible without arm actuation, thereby increasing both opportunity and

* Corresponding author†

**This work was partly supported by the Institute of Information & Communications Technology Planning & Evaluation(IITP)-ITRC(Information Technology Research Center) grant funded by the Korea government(MSIT)(IITP-2025-RS-2024-00437268, 50%) and the National Research Foundation, Singapore, under the NRF Medium Sized Centre scheme (CARTIN, 50%).

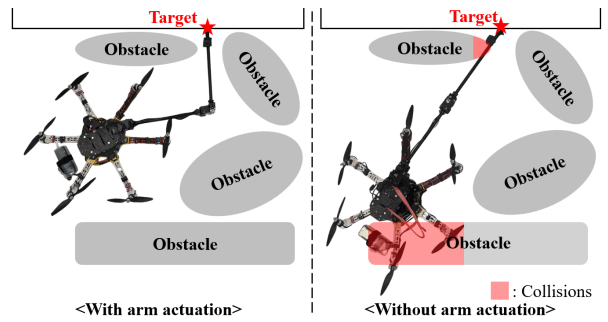


Fig. 1. Robot arm’s actuation for collision avoidance in a cluttered environment.

collision risk. as shown in Fig. 1. Furthermore, in the control level, both dynamic feasibility and instantaneous collision avoidance must be satisfied, as the aerial manipulator may be unable to follow the desired trajectory generated from planners due to the limitations in control performances. However, very few studies have simultaneously addressed collision avoidance between the robot arm’s linkages and surrounding obstacles and the system’s dynamic feasibility.

1.1 Related Works

There have been several studies on collision avoidance of aerial manipulators. In Seo et al. (2017), the authors present a locally optimal trajectory planning method for aerial manipulation in constrained environments, using a signed distance metric and a convex mesh representation to model obstacles. In Cao et al. (2024), the authors propose a motion planning approach for aerial pick-and-place tasks that incorporates collision avoidance constraints between the movable range of the robot arm and surrounding obstacles. Additionally, Zhang et al. (2025) introduces an end-effector-oriented motion planner for aerial manipulators, which accounts for system dynamics and collision avoidance within constrained spaces. However, these methods only focus on the poses of the multirotor and the end-effector, not the collisions between the robot arm’s linkages and obstacles.

To prevent possible collisions between the robot arm’s linkages and the surrounding environment, there exist other studies that investigate collision avoidance methods that explicitly consider the interaction between these linkages and obstacles. Liu et al. (2024) presents a model predictive control framework for safe and compliant aerial manipulation, employing simple box constraints on the states of both the multirotor and the robot arm. Additionally, Lee et al. (2025) proposes a whole-body planning method for omnidirectional aerial manipulators, where both the multirotor platform and the robot arm’s linkages are represented as ellipsoids. Despite these advances, such approaches rely on bounding box or ellipsoid-based geometric representations for aerial manipulators and obstacles, which increase conservativeness when navigating through narrow passages.

To overcome the conservative issue, several studies have developed sampling-based methods for collision avoidance in aerial manipulation. In Kim et al. (2019), the authors present a rapidly-exploring random trees star (RRT*)-based planner for collision-free aerial pick-and-place tasks, and Yavari et al. (2022) introduces an RRT*-based approach that divides operational modes into approach and manipulation phases. However, sampling-based methods are generally more time-consuming than approaches based on geometric representations.

1.2 Contributions

In this paper, we propose a whole-body motion planning and a safety-critical control of an aerial manipulator using superquadrics and proxies, wherein both the multirotor platform and the robot arm’s linkages independently achieve collision avoidance with surrounding obstacles. To this end, we first derive the dynamic model of the aerial manipulator attaching a three degree-of-freedom (DOF) robot arm on a fully actuated hexarotor. Then, we design a maximum-clearance whole-body motion planner by integrating the SQ-proxy representation with Voronoi diagrams on an equilibrium manifold (Campolo and Cardin (2025)). Building upon this planner, a controller complying with propeller thrust limits and collision avoidance is constructed, where the controller framework includes a disturbance observer (DOB)-based control law presented

in Back and Shim (2009). In particular, our main contributions are arranged as follows:

- To the best of the authors’ knowledge, this work is the first to employ a superquadric-proxy representation for aerial manipulators, enabling accurate yet efficient whole-body modeling and differentiable distance evaluation for collision avoidance.
- We design a safety-critical framework that integrates the SQ-proxy representation with Voronoi-based maximum-clearance planning and control barrier functions (CBFs), ensuring dynamic feasibility and instantaneous collision avoidance under thrust limits.
- Comparative simulations and real-world experiments demonstrate that our approach achieves faster, safer, and smoother trajectories than sampling-based planners, while surpassing ellipsoid-based baselines in geometry accuracy.

1.3 Outline

This paper is outlined as follows. In Section 2, we formulate the dynamic model of our fully actuated aerial manipulator, and the path planning method based on superquadrics formulation, Voronoi diagram, and potential function is introduced in Section 3. In Section 4, we present a safety-critical controller guaranteeing thrust limits and instantaneous collision avoidance. Section 5 covers the comparative simulations of the proposed method, and our method is also validated in a real-world experiment with a fully actuated aerial manipulator in Section 6.

1.4 Notations

$\mathbf{0}_{i \times j}$, \mathbf{I}_i , and \mathbf{e}_3 denote the $i \times j$ zero matrix, $i \times i$ identity matrix, and unit vector along the z -axis, respectively; for scalars a_1, \dots, a_N , we use ca_1 and sa_1 for $\cos a_1$ and $\sin a_1$, and $\text{diag}\{a_1, \dots, a_N\}$ for the $N \times N$ diagonal matrix with a_i on the (i, i) -th entry; for vectors $\boldsymbol{\alpha}, \boldsymbol{\beta}$, α_i denotes the i -th element of $\boldsymbol{\alpha}$, and if $\boldsymbol{\alpha}, \boldsymbol{\beta} \in \mathbb{R}^3$, then $[\boldsymbol{\alpha}]_{\times} \in \mathbb{R}^{3 \times 3}$ is the skew-symmetric matrix satisfying $[\boldsymbol{\alpha}]_{\times} \boldsymbol{\beta} = \boldsymbol{\alpha} \times \boldsymbol{\beta}$; for matrices $\mathbf{A}_1, \dots, \mathbf{A}_N$, $\text{blkdiag}\{\mathbf{A}_1, \dots, \mathbf{A}_N\}$ denotes the block diagonal matrix formed by aligning them; and "with respect to" is abbreviated as w.r.t.

2. AERIAL MANIPULATOR SYSTEM

As a platform, we utilize an aerial manipulator configured with a fully actuated multirotor with six tilted motors and a 3-DOF robot arm, as illustrated in Fig. 2. We let \mathcal{F}_W and \mathcal{F}_b denote two key coordinate frames, the Earth-fixed and multirotor body frames, respectively, then the position and ZYX Euler angles of \mathcal{F}_b w.r.t. \mathcal{F}_W are defined as \mathbf{p} and $\boldsymbol{\phi} \in \mathbb{R}^3$, respectively. Since we consider the movement of the robot arm as a part of external disturbances, the generalized coordinate of the aerial manipulator, $\mathbf{q} \in \mathbb{R}^6$, is defined as $[\mathbf{p}; \boldsymbol{\phi}]$.

According to Byun et al. (2025), the Euler-Lagrange model of the aerial manipulator is formulated as follows:

$$\mathbf{M}(\boldsymbol{\phi})\ddot{\mathbf{q}} + \mathbf{C}(\boldsymbol{\phi}, \dot{\boldsymbol{\phi}}) + \mathbf{G} = \boldsymbol{\tau} + \boldsymbol{\tau}_{ext} \quad (1)$$

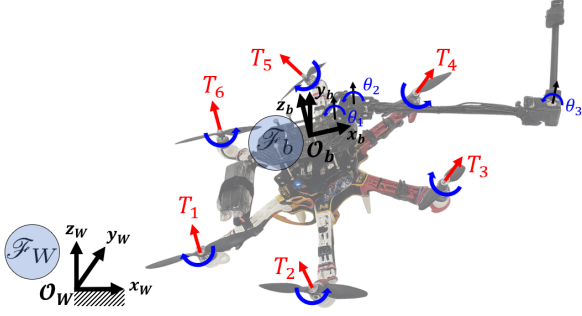


Fig. 2. An aerial manipulator configured with a fully actuated multirotor and a 3-DOF robot arm with the thrust vector, $\mathbf{T} \in \mathbb{R}^6$, the joint angles of the robot arm, $[\theta_1; \theta_2; \theta_3]$, and the Earth-fixed and multirotor frames, \mathcal{F}_W and \mathcal{F}_b .

where $\boldsymbol{\tau}$ and $\boldsymbol{\tau}_{ext} \in \mathbb{R}^6$ represent the generalized control wrench and external disturbances, respectively, and

$$\mathbf{M}(\boldsymbol{\phi}) \triangleq \begin{bmatrix} m\mathbf{I}_3 & \mathbf{0}_{3 \times 3} \\ \mathbf{0}_{3 \times 3} & \mathbf{Q}^\top \mathbf{J} \mathbf{Q} \end{bmatrix},$$

$$\mathbf{C}(\boldsymbol{\phi}, \dot{\boldsymbol{\phi}}) \triangleq \begin{bmatrix} \mathbf{0}_{3 \times 1} \\ \mathbf{Q}^\top (\mathbf{J} \dot{\mathbf{Q}} \dot{\boldsymbol{\phi}} + [\mathbf{Q} \dot{\boldsymbol{\phi}}]_\times \mathbf{J} \mathbf{Q} \dot{\boldsymbol{\phi}}) \end{bmatrix}, \quad \mathbf{G} \triangleq \begin{bmatrix} m g \mathbf{e}_3 \\ \mathbf{0}_{3 \times 1} \end{bmatrix}$$

with the mass and moment of inertia of the aerial manipulator, m and $\mathbf{J} \in \mathbb{R}^{3 \times 3}$, and the gravitational acceleration, g . Also, we let $\mathbf{Q} \in \mathbb{R}^{3 \times 3}$ denote the mapping matrix satisfying $\boldsymbol{\omega} = \mathbf{Q} \dot{\boldsymbol{\phi}}$ where $\boldsymbol{\omega} \in \mathbb{R}^3$ represents the angular velocity of the vehicle w.r.t. \mathcal{F}_W expressed in \mathcal{F}_b . Meanwhile, $\boldsymbol{\tau}$ and $\mathbf{T} \triangleq [T_1; \dots; T_6]$ satisfy:

$$\boldsymbol{\tau} = \mathbf{B}(\boldsymbol{\phi}) \mathbf{T} \quad (2)$$

where

$$\mathbf{B}(\boldsymbol{\phi}) \triangleq \text{blkdiag}\{\mathbf{R}, \mathbf{Q}^\top\}$$

$$\times \begin{bmatrix} \frac{1}{2} s \alpha_p & -s \alpha_p & \frac{1}{2} s \alpha_p & \frac{1}{2} s \alpha_p & -s \alpha_p & \frac{1}{2} s \alpha_p \\ -\frac{\sqrt{3}}{2} s \alpha_p & 0 & \frac{\sqrt{3}}{2} s \alpha_p & -\frac{\sqrt{3}}{2} s \alpha_p & 0 & \frac{\sqrt{3}}{2} s \alpha_p \\ c \alpha_p & c \alpha_p \\ -\frac{1}{2} P_1 & -P_1 & -\frac{1}{2} P_1 & \frac{1}{2} P_1 & P_1 & \frac{1}{2} P_1 \\ \frac{\sqrt{3}}{2} P_1 & 0 & -\frac{\sqrt{3}}{2} P_1 & -\frac{\sqrt{3}}{2} P_1 & 0 & \frac{\sqrt{3}}{2} P_1 \\ P_2 & -P_2 & P_2 & -P_2 & P_2 & -P_2 \end{bmatrix},$$

$$P_1 \triangleq L c \alpha_p + k_f s \alpha_p, \quad P_2 \triangleq L s \alpha_p - k_f c \alpha_p$$

where L , α_p and k_f represent the length from the vehicle's origin to each propeller, fixed tilt angle of each motor and thrust-to-torque coefficient, respectively.

To address the effect of model uncertainties, (1) is rearranged as:

$$\hat{\mathbf{M}}(\boldsymbol{\phi}) \ddot{\boldsymbol{q}} + \hat{\mathbf{C}}(\boldsymbol{\phi}, \dot{\boldsymbol{\phi}}) + \hat{\mathbf{G}} = \boldsymbol{\tau} + \mathbf{d} \quad (3)$$

where $\hat{\mathbf{M}}(\boldsymbol{\phi})$, $\hat{\mathbf{C}}(\boldsymbol{\phi}, \dot{\boldsymbol{\phi}})$ and $\hat{\mathbf{G}}$ are the nominal values of $\mathbf{M}(\boldsymbol{\phi})$, $\mathbf{C}(\boldsymbol{\phi}, \dot{\boldsymbol{\phi}})$ and \mathbf{G} , respectively, and the lumped disturbance $\mathbf{d} \in \mathbb{R}^6$ is derived as follows:

$$\mathbf{d} \triangleq (\hat{\mathbf{M}}(\boldsymbol{\phi}) - \mathbf{M}(\boldsymbol{\phi})) \ddot{\boldsymbol{q}} + \hat{\mathbf{C}}(\boldsymbol{\phi}, \dot{\boldsymbol{\phi}}) - \mathbf{C}(\boldsymbol{\phi}, \dot{\boldsymbol{\phi}}) + \hat{\mathbf{G}} - \mathbf{G} + \boldsymbol{\tau}_{ext}.$$

3. WHOLE-BODY MOTION PLANNING

Building upon Yang et al. (2024, 2025) and Kana et al. (2021), we model the entire aerial manipulator system as well as environmental obstacles using SQs. The interactions between any two SQs are represented by proxies. Meanwhile, the end-effector of the robot arm follows

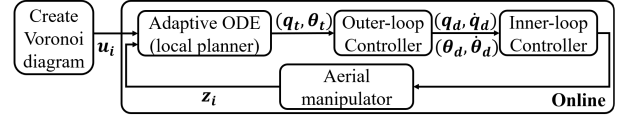


Fig. 3. Overall diagram of planning and control of aerial manipulator.

Voronoi edges, while collision avoidance is also handled via proxies. The entire pipeline is illustrated in Fig. 3.

3.1 Superquadrics and proxies

SQs offer a computationally efficient representation of real-world object geometry (Jaklic et al. (2000)). We define an SQ as follows:

$$F_{3d}(x, y, z) = \left(\left(\frac{x}{a_1} \right)^{\epsilon_2} + \left(\frac{y}{a_2} \right)^{\epsilon_2} \right)^{\epsilon_1} + \left(\frac{z}{a_3} \right)^{\epsilon_1} - 1 \quad (4)$$

where ϵ_1 and ϵ_2 represent the exponents of the 3D superellipse controlling its shape, while a_1, a_2 and a_3 are size-controlling parameters. Also, we introduce the concept of a proxy sliding along the SQ boundary, parameterized by the angular variable $\boldsymbol{\gamma}_{3D}$:

$$\mathbf{p}(\boldsymbol{\gamma}_{3D}) = \begin{bmatrix} a_1 \cos^{\epsilon_1} \boldsymbol{\gamma}_{3D,1} \cos^{\epsilon_2} \boldsymbol{\gamma}_{3D,2} \\ a_1 \cos^{\epsilon_1} \boldsymbol{\gamma}_{3D,1} \sin^{\epsilon_2} \boldsymbol{\gamma}_{3D,2} \\ a_3 \sin^{\epsilon_1} \boldsymbol{\gamma}_{3D,1} \end{bmatrix},$$

$$\boldsymbol{\gamma}_{3D} \in \left[-\frac{\pi}{2}, \frac{\pi}{2} \right] \times [-\pi, \pi] \quad (5)$$

where $\cos^*(\cdot) = \text{sign}(\cos(\cdot)) |\cos(\cdot)|^*$ and $\sin^*(\cdot) = \text{sign}(\sin(\cdot)) |\sin(\cdot)|^*$.

To ensure the safety and stability of the multirotor, excessive tilting is restricted. Under this assumption, the task can be modeled in a 2D scenario. Accordingly, Eqs. 4 and 5 reduce to their 2D formulations, involving only the parameters a_1, a_2, ϵ , and $\gamma \in [-\pi, \pi]$, as presented in Yang et al. (2025).

3.2 Maximum clearance path planning

To enhance the safety of the aerial manipulator system, we adopt the Voronoi diagram as the foundation of our motion planner, since it naturally provides maximal clearance from obstacles in Arslan and Koditschek (2019). Following the approach in Yang et al. (2024), the Voronoi diagram is constructed using SQs and proxies.

(1) *Voronoi diagram* A Voronoi diagram partitions the Euclidean space $E \subset \mathbb{R}^n$ into m regions $\{V_1, V_2, \dots, V_m\}$, commonly referred to as cells. Each cell is defined such that every point within it is closest to the corresponding disjoint convex obstacle SQ (i.e., $d(SQ_i, SQ_j) > 0, \forall i \neq j$). Based on the maximum-margin separating hyperplane, the construction is given by

$$HP_{i,j} := \{ \mathbf{p} \in E \mid \|\mathbf{p} - \mathbf{p}(\boldsymbol{\gamma}_i)\| = \|\mathbf{p} - \mathbf{p}(\boldsymbol{\gamma}_j)\| \}, \quad (6a)$$

$$V_i := \{ \mathbf{p} \in W \mid \|\mathbf{p} - \mathbf{p}(\boldsymbol{\gamma}_i)\| \leq \|\mathbf{p} - \mathbf{p}(\boldsymbol{\gamma}_j)\| \}, \quad (6b)$$

where $HP_{i,j}$ denotes the hyperplane (or boundary) shared by two Voronoi regions V_i and V_j , computed from Eq. 5. Traveling along $HP_{i,j}$ guarantees that the path remains equidistant from the obstacles associated with V_i and V_j , thus forming a so-called maximum-clearance path.

(2) *Global planner* We first define a bounding box (world space W) to appropriately represent the workspace. Consequently, each region V_i is expressed as the intersection

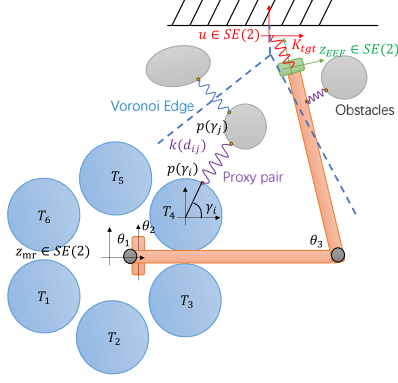


Fig. 4. System representation using SQs and proxies. The end effector of the robot arm aligns with the Voronoi edge to ensure collision-free motion.

of all hyperplanes defining its polyhedral cell within the bounding box:

$$V_i = \bigcup_{j=0}^m W \cap HP_{i,j}. \quad (7)$$

Once all hyperplanes are computed, the Voronoi diagram is represented as a graph $\mathcal{G} = (\mathcal{V}, \mathcal{E})$, where each \mathcal{V}_i corresponds to a polygon defined by multiple vertices and edges. Each vertex is represented as a node $v_i \in \mathcal{V}$, and nodes are connected by edges in \mathcal{E} . The weight assigned to each edge corresponds to the Euclidean distance between its two nodes. Finally, classical graph search algorithms can be applied to compute a solution path, denoted by $(\mathcal{V}_{sol}, \mathcal{E}_{sol})$, consisting of selected nodes, edges, and their orientations.

3.3 Planning on equilibrium manifold

Following Yang et al. (2025); Campolo and Cardin (2025), we formulate the planning task as a manipulation potential function $W : \mathcal{Z} \times \mathcal{U} \rightarrow \mathbb{R}$, where \mathbf{u} denotes the attracting pose of the robotic end effector in control space \mathcal{U} , and \mathbf{z} denotes the state of the aerial manipulator system in state space \mathcal{Z} . The objective is to generate a smooth trajectory such that the end effector reaches the target while the entire system avoids collisions. This problem can be interpreted as finding an equilibrium state \mathbf{z}^* on the *equilibrium manifold* (EM) of the system:

$$\mathcal{M}^{eq} := \{(\mathbf{z}, \mathbf{u}) \in \mathcal{Z} \times \mathcal{U} \mid \partial_{\mathbf{z}} W(\mathbf{z}, \mathbf{u}) = \mathbf{0}\} \quad (8)$$

We define $\partial_{\mathbf{q}} W \equiv [\partial_{q_1} W, \dots, \partial_{q_a} W]^T$, where the *partial operator* is defined as $\partial_{\mathbf{q}} = [\partial_{q_1}, \dots, \partial_{q_a}]^T$. Since the equilibrium state \mathbf{z}^* is implicitly defined, we adopt the adaptive ODE introduced in Yang et al. (2025) to update \mathbf{z}^* , where η represents step size in the ODE :

$$\dot{\mathbf{z}} = -(\partial_{\mathbf{z}\mathbf{z}}^2 W)^{-1} \partial_{\mathbf{u}\mathbf{z}}^2 W \dot{\mathbf{u}} - \eta (\partial_{\mathbf{z}\mathbf{z}}^2 W)^{-1} \partial_{\mathbf{z}} W \quad (9)$$

3.4 System modeling

As illustrated in Fig. 4, the aerial manipulator operates in a 2D space. Define $\mathbf{z}_{mr} \in SE(2)$, and consider a two-link robot arm with two motors rotating along the z -axis with angles θ_1 and θ_3 . The multirotor with six blades is modeled by six SQs, while the two links are modeled by two SQs, resulting in a total of SQ_i , $i = 1, \dots, 8$. Each SQ_i is associated with a proxy pair γ_i, γ_j corresponding to

obstacle SQ_j . Thus, the state variables of the entire system are denoted as $\mathbf{z} = [\mathbf{z}_{sys}, \Gamma]$, where $\mathbf{z}_{sys} = [\mathbf{z}_{mr}, \theta_1, \theta_3]$ represents the combined states of the multirotor and joint, and $\Gamma = [\dots, \gamma_i, \dots, \gamma_j, \dots]$ denotes all proxies. The pose of the end effector $\mathbf{z}_{EEF} \in SE(2)$ is obtained from forward kinematics.

(1) *collision avoidance* The proxy-based potential is used for collision avoidance and proxy dynamics, and is defined as

$$W_{proxy} = \sum_i \sum_j \frac{1}{2} k(d_{ij} - d') \|\mathbf{p}(\gamma_i) - \mathbf{p}(\gamma_j)\|^2 \quad (10)$$

where $d_{ij} = F(j p(\gamma_i))$ represents the evaluation of $p(\gamma_i)$ in the frame of obstacle SQ_j , serving as the 2D version of the inside-outside function in Eq. 4. Here, $k(d)$ is a nonlinear stiffness function: it increases as the multirotor or arm approaches an obstacle and decreases when farther away. The parameter d' specifies the safety margin for obstacle avoidance:

$$k(d) = k_{\min} + \frac{1 - \tanh(d/d_0)}{2} k_{\max}. \quad (11)$$

(2) *Target following* To ensure that the end effector achieves the desired pose, we define an attracting frame $\mathbf{u} = [u_x, u_y, u_\theta] \in SE(2)$, where u_x and u_y follow \mathcal{E}_{sol} , and u_θ aligns with the normal of the Voronoi edge. A virtual spring is applied to connect \mathbf{u} with the end effector \mathbf{z}_{EEF} . The attracting potential is given by

$$W_{tgt} = \frac{1}{2} (\mathbf{u} - \mathbf{z}_{EEF})^T \mathbf{K}_{tgt} (\mathbf{u} - \mathbf{z}_{EEF}) \quad (12)$$

Finally, the manipulation potential is $W = W_{proxy} + W_{tgt}$.

3.5 Local planner

The global planner, based on the Voronoi diagram, returns a set of discrete nodes and edges $(\mathcal{V}_{sol}, \mathcal{E}_{sol})$. Each via point on this path is represented as a discrete attraction pose \mathbf{u}_i . To effectively guide the aerial manipulator system, we require a continuous and smooth reference trajectory $\mathbf{z}^*(s)$, $s \in [0, 1]$. To obtain such a trajectory, we integrate the following augmented ODE system from $s = 0$ to $s = 1$:

$$\frac{\partial \mathbf{u}}{\partial s} = \mathbf{u}_{i+1} - \mathbf{u}_i, \quad (13a)$$

$$\frac{\partial \mathbf{z}_{sys}}{\partial s} = -(\partial_{\mathbf{z}\mathbf{z}}^2 W)^{-1} \partial_{\mathbf{u}\mathbf{z}}^2 W \frac{\partial \mathbf{z}_{sys}}{\partial s} - \eta (\partial_{\mathbf{z}\mathbf{z}}^2 W)^{-1} \partial_{\mathbf{z}} W, \quad (13b)$$

$$\frac{\partial \Gamma}{\partial s} = -\alpha \partial_{\Gamma} W, \quad (13c)$$

where initial condition comes from the aerial manipulator's current state.

3.6 Target Pose Calculation

From the results of the local planner, the target pose of the multirotor, \mathbf{q}_t , and the target angles of the robot arm's servo motors, θ_t , are calculated as follows:

$$\begin{aligned} \mathbf{q}_t &= [z_{sys,1}(s(t)); z_{sys,2}(s(t)); h_t; 0; 0; z_{sys,3}(s(t))] \\ \theta_t &= [z_{sys,4}(s(t)); 0; z_{sys,5}(s(t))] \end{aligned} \quad (14)$$

where the time allocated path parameter $s(t)$ is calculated as $\frac{1}{T_d} t$ with the desired task execution time $T_d > 0$, and h_t represents the target altitude of the multirotor.

4. SAFETY-CRITICAL CONTROLLER

This section presents a safety-critical controller that tracks the desired trajectories of both the multirotor and the robot arm, subject to two safety constraints. The first constraint enforces propeller-thrust limits: when \mathbf{q}_t is substantially far from the current pose \mathbf{q} , the required control effort can drive one or more rotor thrust beyond their physical bounds. The second constraint enforces instantaneous collision avoidance. This addresses cases where tracking errors between $(\mathbf{q}, \boldsymbol{\theta})$ and $(\mathbf{q}_t, \boldsymbol{\theta}_t)$ arises due to limited control authority, even when the planned global path is collision-free. As depicted in Fig. 3, the proposed controller is divided into two sequences: outer- and inner-loop control laws.

4.1 Inner-Loop Control Law

To cope with three performance deteriorating factors, i.e., movement of the attached robot arm, model uncertainties, and time-varying external disturbance, we adopt a DOB-based controller extending the control law introduced in Kim et al. (2017) to incorporate 6 DOF pose.

Let \mathbf{q}_d and $\boldsymbol{\theta}_d$ denote the desired pose of the multirotor and the desired joint angles of the robot arm, respectively, which the multirotor and robot arm attempt to track. However, these may differ from the target values, \mathbf{q}_t and $\boldsymbol{\theta}_t$, since an *outer-loop controller* is also designed to adjust the target values in accordance with the safety constraints. This controller will be introduced in a later subsection.

With \mathbf{q}_d and $\boldsymbol{\theta}_d$, our inner-loop control law is formulated as follows:

$$\begin{aligned} \mathbf{T} &= \mathbf{B}^{-1}(\phi) \{ \hat{\mathbf{M}}(\phi) (\mathbf{K}_d \dot{\mathbf{e}} + \mathbf{K}_p \mathbf{e}) \\ &\quad + \hat{\mathbf{C}}(\phi, \dot{\phi}) + \hat{\mathbf{G}} - \hat{\mathbf{d}} \} \\ \hat{\mathbf{d}} &= -\hat{\mathbf{M}}(\phi) (\mathbf{E}_1 \mathbf{p}_{dob} - \mathbf{E}_2 \dot{\mathbf{q}}_{dob}) + \hat{\mathbf{C}}(\phi, \dot{\phi}) + \hat{\mathbf{G}} \\ \dot{\mathbf{q}}_{dob} &= \mathbf{A}_{dob} \mathbf{q}_{dob} + \mathbf{B}_{dob} \mathbf{q} \\ \dot{\mathbf{p}}_{dob} &= \mathbf{A}_{dob} \mathbf{p}_{dob} + \mathbf{B}_{dob} \mathbf{M}^{-1}(\phi) \mathbf{B}(\phi) \mathbf{T} \end{aligned} \quad (15)$$

where $\mathbf{e} \triangleq \mathbf{q}_d - \mathbf{q}$, $\mathbf{E}_1 \triangleq [\mathbf{I}_6 \ \mathbf{0}_{6 \times 6}]$ and $\mathbf{E}_2 \triangleq [\mathbf{0}_{6 \times 6} \ \mathbf{I}_6]$ with user-defined positive definite matrices $\mathbf{K}_p, \mathbf{K}_d \in \mathbb{R}^{6 \times 6}$. Also, $\hat{\mathbf{d}}$ represents the estimated lumped disturbance, and

$$\mathbf{A}_{dob} \triangleq \begin{bmatrix} \mathbf{0}_{6 \times 6} & \mathbf{I}_6 \\ -\varepsilon_{dob}^{-2} \mathbf{a}_0 & -\varepsilon_{dob}^{-1} \mathbf{a}_1 \end{bmatrix}, \quad \mathbf{B}_{dob} \triangleq \begin{bmatrix} \mathbf{0}_{6 \times 6} \\ \varepsilon_{dob}^{-2} \mathbf{a}_0 \end{bmatrix}$$

with user-defined matrices $\mathbf{a}_0 \triangleq \text{diag}\{a_{0,1}, \dots, a_{0,6}\}$, $\mathbf{a}_1 \triangleq \text{diag}\{a_{1,1}, \dots, a_{1,6}\}$ and $\varepsilon_{dob} \triangleq \text{diag}\{\varepsilon_{dob,1}, \dots, \varepsilon_{dob,6}\}$ under $0 < a_{0,i}, a_{1,i}, \frac{1}{2} < \frac{a_{0,i}}{a_{1,i}^2}$ and $0 < \varepsilon_{dob,i} < 1 \ \forall i = 1, \dots, 6$.

4.2 Safety Constraints

The two safety conditions are formulated as follows:

(1) *Thrust Limit* The thrust values have their lower and upper limits, $\underline{\mathbf{T}}$ and $\bar{\mathbf{T}}$, as follows:

$$\underline{\mathbf{T}} \mathbf{1}_6 \leq \mathbf{T} \leq \bar{\mathbf{T}} \mathbf{1}_6 \quad (16)$$

where $\mathbf{1}_6 \triangleq [1 \ 1 \ 1 \ 1 \ 1 \ 1]^\top$. If one of the propellers reaches its limit, the multirotor may lose controllability.

(2) *Collision Avoidance* To compensate for possible target-tracking errors in the proposed inner-loop controller, an additional strategy at the control level is necessary for collision avoidance, depending on the aerial manipulator's pose and the robot arm's joint angles in real time.

To derive a mathematical expression for this constraint, we utilize superquadrics as defined in Eq.4. For SQ_i (one of the *vehicle* SQs) and SQ_j (one of the *obstacle* SQs) ($i = 1, \dots, 8, j = 1, \dots, m$), the closest points follows Eq. 5. We let $\Delta \mathbf{X} \in \mathbb{R}^3$ denote the displacement from the center of SQ_j to the proxy of SQ_i as follows:

$$\begin{aligned} \Delta \mathbf{X} &\triangleq [\Delta x; \Delta y; \Delta z] \\ &\triangleq \mathbf{R}_j^\top (\mathbf{p}_i - \mathbf{p}_j) + \mathbf{R}_j^\top \mathbf{R}_i \mathbf{p}(\gamma_{3D,i}) \end{aligned} \quad (17)$$

where \mathbf{R}_i and $\mathbf{R}_j \in SO(3)$ represent the rotation matrices from SQ_i to \mathcal{F}_W and from SQ_j to \mathcal{F}_W , respectively, \mathbf{p}_i and $\mathbf{p}_j \in \mathbb{R}^3$ mean the displacement from \mathcal{F}_W to the centers of SQ_i and SQ_j , respectively, and $\gamma_{3D,i}$ is the angular variable of SQ_i . Then, a control barrier function (CBF) for collision avoidance is defined as follows:

$$h_{co} \triangleq \ln \left(\left(\left(\frac{\Delta x}{j_{a_1}} \right)^{\frac{2}{j_{\epsilon_2}}} + \left(\frac{\Delta y}{j_{a_2}} \right)^{\frac{2}{j_{\epsilon_2}}} \right)^{\frac{j_{\epsilon_2}}{j_{\epsilon_1}}} + \left(\frac{\Delta z}{j_{a_3}} \right)^{\frac{2}{j_{\epsilon_1}}} \right) \quad (18)$$

where $j_{\epsilon_1}, j_{\epsilon_2}, j_{a_1}, j_{a_2}$ and j_{a_3} are the parameters of SQ_j .

According to Eq. 18, h_{co} becomes positive when the proxy of SQ_i is located outside the SQ_j ; namely, two SQs do not collide. Thus, h_{co} can be a CBF for the collision avoidance.

4.3 Outer-Loop Control Law

Given the target pose of the aerial manipulator from Eq. 14, the desired pose and twist, $[\mathbf{q}_d; \boldsymbol{\theta}_d]$ and $[\dot{\mathbf{q}}_d; \dot{\boldsymbol{\theta}}_d]$, need to be generated based on the two safety conditions.

For the thrust limits, we rearrange Eq. 16 as follows:

$$\mathbf{A}_T \dot{\mathbf{q}}_d \leq \mathbf{b}_T, \quad \mathbf{A}_{\bar{T}} \dot{\mathbf{q}}_d \leq \mathbf{b}_{\bar{T}}, \quad (19)$$

where $\mathbf{A}_T \triangleq -\mathbf{B}^{-1}(\phi) \hat{\mathbf{M}}(\phi) \mathbf{K}_d$, $\mathbf{A}_{\bar{T}} \triangleq -\mathbf{A}_T$ and

$$\begin{aligned} \mathbf{b}_T &\triangleq -\underline{\mathbf{T}} \mathbf{1}_6 + \mathbf{B}^{-1}(\phi) \\ &\quad \times [\hat{\mathbf{M}}(\phi) \{ -\mathbf{K}_d \dot{\mathbf{q}} + \mathbf{K}_p \mathbf{e} \} + \hat{\mathbf{C}}(\phi, \dot{\phi}) + \hat{\mathbf{G}} - \hat{\mathbf{d}}], \\ \mathbf{b}_{\bar{T}} &\triangleq \bar{\mathbf{T}} \mathbf{1}_6 - \mathbf{B}^{-1}(\phi) \\ &\quad \times [\hat{\mathbf{M}}(\phi) \{ -\mathbf{K}_d \dot{\mathbf{q}} + \mathbf{K}_p \mathbf{e} \} + \hat{\mathbf{C}}(\phi, \dot{\phi}) + \hat{\mathbf{G}} - \hat{\mathbf{d}}] \end{aligned}$$

Meanwhile, since h_{co} is the function of $(\mathbf{q}, \boldsymbol{\theta})$, we need to differentiate it twice to attain the thrust inputs. Hence, Eq. 18 becomes a high-order CBF (Xiao and Belta (2021)), and the collision avoidance condition is formulated as follows:

$$\ddot{h}_{co} + 2\alpha_{co} \dot{h}_{co} + \alpha_{co}^2 h_{co} \geq 0 \quad (20)$$

where $\alpha_{co} > 0$ is a user-defined parameter. With the assumption that $\gamma_{3D,i}$ and $\gamma_{3D,j}$ slowly change with time, the time-derivatives of h_{co} depend on those of \mathbf{p}_i and \mathbf{R}_i . Therefore, \ddot{h}_{co} and \dot{h}_{co} can be expressed as follows:

$$\begin{aligned} \dot{h}_{co} &= \frac{\partial h_{co}}{\partial \Delta \mathbf{X}} (\Delta \dot{\mathbf{X}}) \\ \ddot{h}_{co} &= \frac{\partial h_{co}}{\partial \Delta \mathbf{X}} (\Delta \ddot{\mathbf{X}}) + (\Delta \dot{\mathbf{X}})^\top \frac{\partial^2 h_{co}}{\partial (\Delta \mathbf{X})^2} (\Delta \dot{\mathbf{X}}). \end{aligned} \quad (21)$$

where we can find matrices $\mathbf{A}_{\Delta \mathbf{X}} \in \mathbb{R}^{3 \times 9}$ and $\mathbf{b}_{\Delta \mathbf{X}} \in \mathbb{R}^3$ such that $(\Delta \dot{\mathbf{X}}) = \mathbf{A}_{\Delta \mathbf{X}} [\dot{\mathbf{q}}; \dot{\boldsymbol{\theta}}] + \mathbf{b}_{\Delta \mathbf{X}}$ from Eq. 17. Also, by substituting Eq. 15 for Eq. 3, $\dot{\mathbf{q}}$ is rearranged as follows:

$$\dot{\mathbf{q}} = \mathbf{K}_d \dot{\mathbf{q}}_d - \mathbf{K}_d \dot{\mathbf{q}} + \mathbf{K}_p \mathbf{e} - \hat{\mathbf{M}}^{-1}(\phi) \hat{\mathbf{d}} \quad (22)$$

where $\tilde{\mathbf{d}} \triangleq \hat{\mathbf{d}} - \mathbf{d}$. Assume that $\tilde{\boldsymbol{\theta}} \approx \tilde{\boldsymbol{\theta}}_d$, then (20) is rearranged as follows:

$$\mathbf{A}_{co}[\dot{\mathbf{q}}_d; \ddot{\boldsymbol{\theta}}_d] + d_{co} \leq b_{co} \quad (23)$$

where

$$\begin{aligned} \mathbf{A}_{co} &\triangleq -\frac{\partial h_{co}}{\partial \Delta \mathbf{X}} \mathbf{A}_{\Delta \mathbf{X}} \begin{bmatrix} \mathbf{K}_d & \mathbf{0}_{6 \times 3} \\ \mathbf{0}_{3 \times 6} & \mathbf{I}_3 \end{bmatrix}, \\ d_{co} &\triangleq \frac{\partial h_{co}}{\partial \Delta \mathbf{X}} \mathbf{A}_{\Delta \mathbf{X}} \begin{bmatrix} \hat{\mathbf{M}}^{-1}(\phi) \tilde{\mathbf{d}} \\ \mathbf{0}_{3 \times 1} \end{bmatrix}, \\ b_{co} &\triangleq \frac{\partial h_{co}}{\partial \Delta \mathbf{X}} \mathbf{A}_{\Delta \mathbf{X}} \begin{bmatrix} -\mathbf{K}_d \dot{\mathbf{q}} + \mathbf{K}_p \mathbf{e} \\ \mathbf{0}_{3 \times 1} \end{bmatrix} + \frac{\partial h_{co}}{\partial \Delta \mathbf{X}} \mathbf{b}_{\Delta \mathbf{X}} + \\ &(\Delta \dot{\mathbf{X}})^\top \frac{\partial^2 h_{co}}{\partial (\Delta \mathbf{X})^2} (\Delta \dot{\mathbf{X}}) + 2\alpha_{co} \frac{\partial h_{co}}{\partial \Delta \mathbf{X}} (\Delta \dot{\mathbf{X}}) + \alpha_{co}^2 h_{co}. \end{aligned}$$

As d_{co} contains the disturbance estimation error, a more conservative collision avoidance constraint is expressed as:

$$\mathbf{A}_{co}[\dot{\mathbf{q}}_d; \ddot{\boldsymbol{\theta}}_d] + \sigma_{co} \leq b_{co} \quad (24)$$

where $|d_{co}| \leq \sigma_{co}$.

Finally, a quadratic programming (QP)-based outer-loop controller is constructed as follows:

$$\begin{aligned} \min_{[\dot{\mathbf{q}}_d; \ddot{\boldsymbol{\theta}}_d]} & \|\dot{\mathbf{q}}_d - \dot{\mathbf{q}}_{d,ref}\|_{\mathbf{Q}_{\dot{\mathbf{q}}}}^2 + \|\ddot{\boldsymbol{\theta}}_d - \ddot{\boldsymbol{\theta}}_{d,ref}\|_{\mathbf{Q}_{\ddot{\boldsymbol{\theta}}}}^2 \\ \text{s.t.} & \text{Eq. 19 and Eq. 24} \end{aligned} \quad (25)$$

where $\dot{\mathbf{q}}_{d,ref} \triangleq \boldsymbol{\Gamma}_q(\mathbf{q}_t - \mathbf{q}_d)$ and $\ddot{\boldsymbol{\theta}}_{d,ref} \triangleq -2\boldsymbol{\Gamma}_\theta \dot{\boldsymbol{\theta}}_d + \boldsymbol{\Gamma}_\theta^2(\boldsymbol{\theta}_t - \boldsymbol{\theta}_d)$ with weight matrices $\mathbf{Q}_{\dot{\mathbf{q}}}, \mathbf{Q}_{\ddot{\boldsymbol{\theta}}} \in \mathbb{R}_{>0}^{3 \times 3}$, and target-following coefficients $\boldsymbol{\Gamma}_q, \boldsymbol{\Gamma}_\theta \in \mathbb{R}_{>0}^{3 \times 3}$. Then, the desired pose and joint angles are obtained by integration.

5. SIMULATION RESULTS

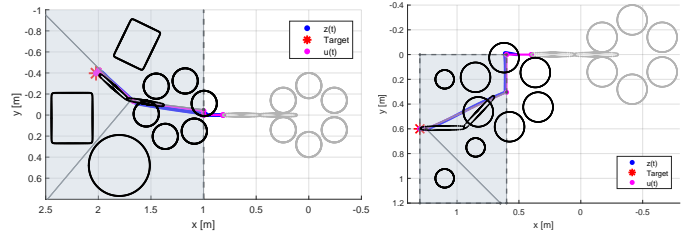
We first evaluate the proposed planner in simulation. Two representative scenarios with various initial conditions are tested, and the results are compared against several typical and widely used baseline planners.

5.1 Results from whole-body motion planner

The results from the whole-body motion planner are shown in Fig. 5, where the two scenarios correspond to environments with trees and pillars respectively. These scenarios are designed such that the target can only be reached by exploiting the thin linkages of the robot arm, thereby validating the necessity of whole-body planning.

5.2 Benchmark

We compare our method against two widely used sampling-based algorithms: RRT* (Karaman and Frazzoli (2011)) and Model Predictive Path Integral control (MPPI) (Williams et al. (2017)), as well as an ablation study that replaces SQs with ellipses for obstacle modeling. The comparisons are illustrated in Fig. 6 and Table 1. In the implementation, RRT* is sampled in \mathbf{z}_{sys} , with collision detection based on the geometric overlap between the aerial manipulator and obstacles at each configuration \mathbf{z} . MPPI is evaluated with a cost function that penalizes both target distance and trajectory smoothness, using $N = 50$ rollouts per control step, which provides a trade-off between computational cost and trajectory quality. The ablation study adopts the same settings as the proposed



(a) Tree-like obstacles. (b) Pillar-like obstacles.

Fig. 5. Simulation results from the whole-body motion planner. Blue transparent polygons represent Voronoi regions V_i separated by grey hyperplanes $HP_{i,j}$, computed via proxies between obstacles. The aerial manipulator and obstacles are modeled by SQs (black). The red point denotes the target; magenta indicates $\mathbf{u}(s)$ during ODE integration (Eq. 13); and blue shows the smooth trajectory $\mathbf{z}(s)$ of the aerial manipulator.

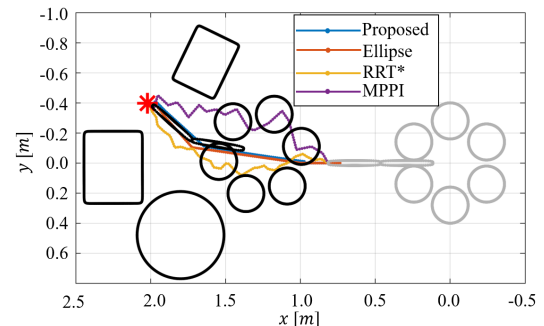


Fig. 6. Comparison of end-effector trajectories by different planners: (a) the proposed SQ-based planner, (b) ablation study (ellipses) (c) RRT*, (d) MPPI.

Table 1. Benchmark with related planners

Method	Time	Min-distance	Arc-length	Jerkiness
Proposed	0.128	0.0644	1.375	0.0016
Ellipse	0.113	-0.0049	1.383	0.0001
RRT*	105.8	0.0314	1.565	0.0032
MPPI	0.552	0.0039	1.721	0.0057

algorithm, except that obstacles are represented as ellipses instead of SQs.

We evaluate four performance metrics, as summarized in Table 1: i) Time denotes the online computational cost. For our method, this is the time to integrate Eq. 13. For MPPI, it corresponds to the time required for one receding-horizon planning cycle (i.e., one control update step). For RRT*, it is the average time needed to generate a collision-free path. ii) Minimum distance represents the closest distance between the robot system and obstacles. Our SQ-based method achieves maximum clearance, thus yielding the safest trajectories. In contrast, the ellipse-based ablation tends to overestimate obstacle sizes, which can trigger unnecessary avoidance maneuvers. This difference is particularly evident in cluttered environments. iii) Arc-length measures the total trajectory length. Shorter arc-length indicates a more efficient path. iv) Jerkiness quantifies trajectory smoothness. A lower value indicates a smoother motion, which is critical for stability.

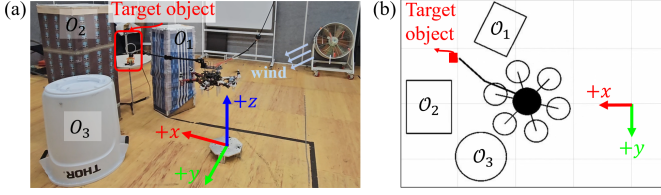


Fig. 7. Flight experiment setup: (a) 3D side view in the laboratory environment. An industrial fan is utilized to simulate wind conditions. (b) 2D top view illustration.

6. EXPERIMENTAL RESULTS

We also validate our planner and controller with an actual object-picking experiment using our aerial manipulator. Fig. 7 displays our experimental setting.

6.1 Experimental Setups

The aerial manipulation platform combines a fully actuated hexacopter and a 3-DOF robot arm. The 3.50 kg hexacopter, based on a DJI F550 frame, uses six 9-inch APC LPB09045MR propellers, KDE2314XF-965 motors with KDEXF-UAS35 ESCs, and custom 3D-printed thrust-tilting mounts set at $\alpha_p = 15^\circ$. Power is supplied by separate 4S (Intel NUC) and 6S (ESC) LiPo batteries. The arm uses three ROBOTIS Dynamixel XM430 actuators via a U2D2 interface. An Intel NUC running Ubuntu 20.04 and ROS Noetic handles control and OptiTrack-based navigation, while motor speeds are governed by a custom Pixhawk 4. An industrial fan is utilized to simulate wind conditions, and the parameter values are listed in Table 2.

Table 2. Parameters for planner and controller

α_p, L, k_f	$\frac{\pi}{12}$ [rad], 0.278 m, 0.016 m
α, T_d, d_0	20 [-], 30 s, 1.0 mm
(k_{\min}, k_{\max})	$(1.0 \times 10^{-7}, 1.0 \times 10^3)$ N/m
\mathbf{K}_{tgt}	$800 \text{diag}\{2.0, 2.0, 1.0\}$ [-]
$\mathbf{a}_0, \mathbf{a}_1, \varepsilon_{dob}$	$\mathbf{I}_6, 2\mathbf{I}_6, 0.95\mathbf{I}_6$ [-]
$\alpha_{co}, \sigma_{co}, \underline{T}, \bar{T}$	5.0 [-], 1.0 [-], 1.0 N, 15 N
$\mathbf{Q}_q, \mathbf{Q}_{\dot{q}}, \mathbf{\Gamma}_q, \mathbf{\Gamma}_\theta$	$\text{blkdiag}\{\mathbf{I}_3, 3\mathbf{I}_3\}, 4\mathbf{I}_3, 4\mathbf{I}_6, 5\mathbf{I}_3$ [-]
\mathbf{K}_p	$\text{blkdiag}\{6\mathbf{I}_2, 8.0, 80\mathbf{I}_2, 35\}$ [-]
\mathbf{K}_d	$\text{blkdiag}\{5\mathbf{I}_2, 6.0, 35\mathbf{I}_2, 20\}$ [-]

As illustrated in Fig. 7(a), obstacle 1 is a blue cuboid (0.4 m \times 0.31 m \times 1.03 m), obstacle 2 is a brown cuboid (0.48 m \times 0.39 m \times 1.27 m), and obstacle 3 is a white cylinder (radius 0.29 m, height 0.72 m). The poses of all obstacles and the target object are measured using the OptiTrack motion capture system.

6.2 Scenario

The aerial manipulator takes off and deploys the robot arm to its fully extended configuration ($\boldsymbol{\theta} = \mathbf{0}_{3 \times 1}$). Subsequently, the path planning algorithm is activated, after which the vehicle follows the generated trajectory, guides the end-effector through the ring affixed to the target, ascends to grasp it, and returns to the initial position.

6.3 Result and Discussion

Figs. 8 and 9 indicate that the task is completed without collisions. In Fig. 8, h_{co} remains positive throughout the

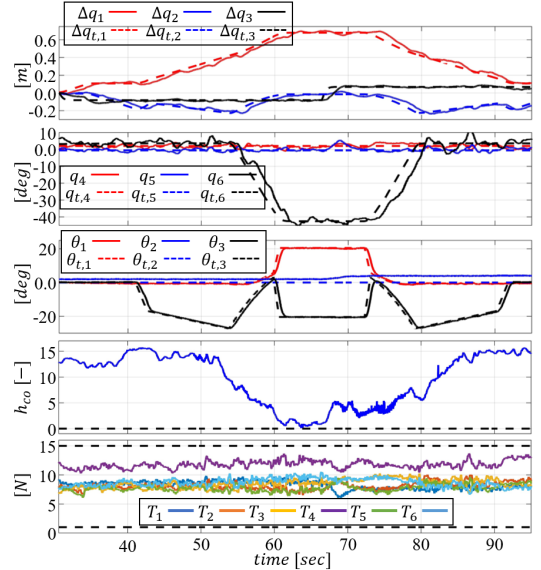


Fig. 8. Histories of the multirotor's measured and target displacements from initial position ($[\Delta q_1; \Delta q_2; \Delta q_3] \triangleq [q_1 - q_1(t_0); q_2 - q_2(t_0); q_3 - q_3(t_0)]$ and $[\Delta q_{t,1}; \Delta q_{t,2}; \Delta q_{t,3}] \triangleq [q_{t,1} - q_{t,1}(t_0); q_{t,2} - q_{t,2}(t_0); q_{t,3} - q_{t,3}(t_0)]$), multirotor's measured and target Euler angles ($[q_4; q_5; q_6]$ and $[q_{t,4}; q_{t,5}; q_{t,6}]$), robot arm's measured and target joint angles ($\boldsymbol{\theta}$ and $\boldsymbol{\theta}_t$), collision avoidance CBF, h_{co} , and thrust values during approaching, picking, and returning.

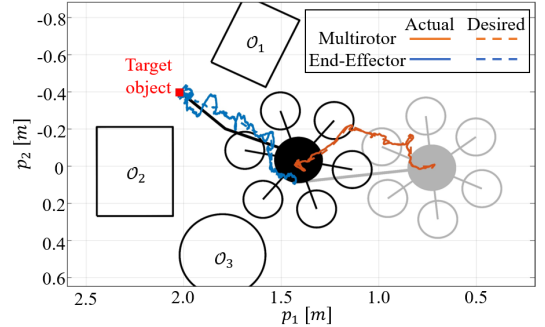


Fig. 9. 2D top view trajectories of the multirotor and the end-effector from the initial to picking poses.

operation, confirming collision-free performance despite tracking errors in the multirotor's position and attitude, and all motor thrusts adhere to their limits. These results verify the effectiveness of our controller for instantaneous collision avoidance. Fig. 9 displays the multirotor navigating and rotating within a narrow path, while the robot arm simultaneously bends to reach the target object. The attached video (<https://youtu.be/hQYKwrWf1Ak>) presents not only a more detailed visualization of the experimental process, but also illustrates how the CBF intervenes to block the target-approaching behavior.

7. CONCLUSION

This paper proposes whole-body motion planning and safety-critical control for an aerial manipulator using superquadrics and proxies, where both the multirotor platform and the robot arm linkages independently avoid collisions with surrounding obstacles. First, we derive the dynamic model of the aerial manipulator by attaching a

multi-DOF robot arm to a fully actuated hexarotor. Second, we design a maximum-clearance whole-body motion planner by integrating the SQ-proxy representation with Voronoi diagrams on an equilibrium manifold. Third, a controller is developed to ensure thrust limits and collision avoidance. Through comparative simulations, we show that our framework outperforms sampling-based planners in cluttered environments, achieving faster, safer, and smoother trajectories, and surpasses ellipsoid-based ablation methods in accurately representing geometry. Additionally, we validate the dynamic feasibility and robustness of our approach on a physical aerial manipulator.

For future work, both the planning and control methods will be extended to three-dimensional environments and experimentally validated in more cluttered scenarios that include thin cylindrical obstacles only allowing narrow gaps near the target location.

REFERENCES

- Arslan, O. and Koditschek, D.E. (2019). Sensor-based reactive navigation in unknown convex sphere worlds. *The International Journal of Robotics Research*, 38(2-3), 196–223.
- Back, J. and Shim, H. (2009). An inner-loop controller guaranteeing robust transient performance for uncertain mimo nonlinear systems. *IEEE Transactions on Automatic Control*, 54(7), 1601–1607.
- Blöchlinger, M., Toshimitsu, Y., and Katzschnmann, R.K. (2025). Reliable aerial manipulation: Combining visual tracking with range sensing for robust grasping. In *2025 IEEE International Conference on Robotics and Automation (ICRA)*, 7519–7525. IEEE.
- Byun, J., Kim, Y., Lee, D., and Kim, H.J. (2025). Safety-critical control for aerial physical interaction in uncertain environment. In *2025 IEEE International Conference on Robotics and Automation (ICRA)*, 7526–7532. IEEE.
- Byun, J., Lee, D., Seo, H., Jang, I., Choi, J., and Kim, H.J. (2021). Stability and robustness analysis of plug-pulling using an aerial manipulator. In *2021 IEEE/RSJ International Conference on Intelligent Robots and Systems (IROS)*, 4199–4206. IEEE.
- Campolo, D. and Cardin, F. (2025). A geometric framework for quasi-static manipulation of a network of elastically connected rigid bodies. *Applied Mathematical Modelling*, 143, 116003.
- Cao, H., Shen, J., Liu, C., Zhu, B., and Zhao, S. (2024). Motion planning for aerial pick-and-place with geometric feasibility constraints. *IEEE Transactions on Automation Science and Engineering*, 22, 2577–2594.
- D’Angelo, S., Marcellini, S., De Crescenzo, A., Marolla, M., Lippiello, V., and Siciliano, B. (2025). A semi-autonomous aerial platform enhancing non-destructive tests. *Drones*, 9(8), 516.
- Jaklic, A., Leonardis, A., and Solina, F. (2000). *Segmentation and recovery of superquadrics*, volume 20. Springer Science & Business Media.
- Kana, S., Tee, K.P., and Campolo, D. (2021). Human-robot co-manipulation during surface tooling: A general framework based on impedance control, haptic rendering and discrete geometry. *Robotics and Computer-Integrated Manufacturing*, 67, 102033.
- Karaman, S. and Frazzoli, E. (2011). Sampling-based algorithms for optimal motion planning. *The international journal of robotics research*, 30(7), 846–894.
- Kim, H., Seo, H., Kim, J., and Kim, H.J. (2019). Sampling-based motion planning for aerial pick-and-place. In *2019 IEEE/RSJ International Conference on Intelligent Robots and Systems (IROS)*, 7402–7408. IEEE.
- Kim, S., Choi, S., Kim, H., Shin, J., Shim, H., and Kim, H.J. (2017). Robust control of an equipment-added multirotor using disturbance observer. *IEEE Transactions on Control Systems Technology*, 26(4), 1524–1531.
- Lee, D., Kim, B., and Kim, H.J. (2025). Autonomous aerial manipulation at arbitrary pose in se (3) with robust control and whole-body planning. *arXiv preprint arXiv:2508.19608*.
- Lee, D., Seo, H., Kim, D., and Kim, H.J. (2020). Aerial manipulation using model predictive control for opening a hinged door. In *2020 IEEE International Conference on Robotics and Automation (ICRA)*, 1237–1242. IEEE.
- Liu, Q., Lyu, S., Guo, K., Wang, J., Yu, X., and Guo, L. (2024). A coordinated framework of aerial manipulator for safe and compliant physical interaction. *Control Engineering Practice*, 146, 105898.
- Seo, H., Kim, S., and Kim, H.J. (2017). Locally optimal trajectory planning for aerial manipulation in constrained environments. In *2017 IEEE/RSJ International Conference on Intelligent Robots and Systems (IROS)*, 1719–1724. IEEE.
- Susbielle, P., Dumon, J., and Hably, A. (2025). Pointillism wall painting drone using bouncing frequency control. *IEEE Robotics and Automation Letters*.
- Williams, G., Wagener, N., Goldfain, B., Drews, P., Rehg, J.M., Boots, B., and Theodorou, E.A. (2017). Information theoretic mpc for model-based reinforcement learning. In *2017 IEEE international conference on robotics and automation (ICRA)*, 1714–1721. IEEE.
- Xiao, W. and Belta, C. (2021). High-order control barrier functions. *IEEE Transactions on Automatic Control*, 67(7), 3655–3662.
- Yang, L., Iyer, G., Lou, B., Turlapati, S.H., Lv, C., and Campolo, D. (2024). Path planning in complex environments with superquadrics and voronoi-based orientation. *arXiv preprint arXiv:2411.05279*.
- Yang, L., Turlapati, S.H., Lv, C., and Campolo, D. (2025). Planning for quasi-static manipulation tasks via an intrinsic haptic metric: A book insertion case study. *IEEE Robotics and Automation Letters*.
- Yavari, M., Gupta, K., and Mehrandezh, M. (2022). Interleaved predictive control and planning for an unmanned aerial manipulator with on-the-fly rapid re-planning in unknown environments. *IEEE Transactions on Automation Science and Engineering*, 20(3), 1690–1705.
- Zhang, Z., Yu, H., Chai, Y., Yang, Z., Liang, X., Fang, Y., and Han, J. (2025). An end-effector-oriented coupled motion planning method for aerial manipulators in constrained environments. *IEEE/ASME Transactions on Mechatronics*.